
Article:
Bokshi, A., Dickinson, D. orcid.org/0000-0002-0868-211X, Roach, C. M. et al. (1 more author) (2016) The response of toroidal drift modes to profile evolution : A model for small-ELMs in tokamak plasmas? Plasma Physics and Controlled Fusion. 075011. pp. 1-13. ISSN 1361-6587

https://doi.org/10.1088/0741-3335/58/7/075011

The response of toroidal drift modes to profile evolution: a model for small-ELMs in tokamak plasmas?

A Bokshi[1], D Dickinson[1], C M Roach[2] and H R Wilson[1]

[1] York Plasma Institute, Department of Physics, University of York, Heslington, York YO10 5DD, UK

[2] CCFE Culham Science Centre, Abingdon, Oxon OX14 3DB, UK

E-mail: ab1209@york.ac.uk

Abstract. We consider a time-dependent linear global electrostatic toroidal fluid ion-temperature gradient (ITG) model to study the evolution of toroidal drift modes in tokamak plasmas as the equilibrium flow-shear varies with time. While we consider the ITG mode as a specific example, the results are expected to be valid for most other toroidal microinstabilities. A key result is that when there is a position in the plasma with a maximum in the instability drive (e.g. ITG), there is a transient burst of stronger growth as the flow-shear evolves through a critical value. This transient burst is expected to drive a filamentary plasma eruption, reminiscent of small-ELMs. The amplitude of the dominant linear mode is initially peaked above or below the outboard midplane, and rotates through it poloidally as the flow-shear passes through the critical value. This theoretical prediction could provide an experimental test of whether this mechanism underlies some classes of small-ELMs.

PACS numbers: 52.55.-s

Keywords: Toroidal drift modes, small-ELMs, Ballooning formalism, Floquet Modes

Submitted to: *Plasma Phys. Control. Fusion*

1. Introduction

The optimisation of heat and particle losses caused by turbulent transport is regarded as one of the main research areas in the pursuit of magnetic confinement fusion as a commercial source of energy. This plasma turbulence is driven by microinstabilities - a class of plasma instabilities with wavelengths perpendicular to the magnetic field line of the order of the ion Larmor radius. These can be electrostatic or electromagnetic in nature, and arise from the destabilisation of basic plasma waves. To provide a specific example, we will focus on an electrostatic ion-temperature gradient (ITG) mode associated with the sound wave. Nevertheless, from previous analytic theory

[1–3], we expect our analysis and conclusions to be generic to most other toroidal microinstabilities.

While a full calculation of the turbulence saturation level must involve non-linear effects, linear studies of the candidate modes provide a helpful insight into understanding the conditions and some consequences of turbulence. For example, turbulent transport is often sufficiently stiff to ensure the density and temperature profiles adjust close to the threshold predicted by linear theory [4, 5].

Toroidal drift instabilities are characterised by short wavelengths perpendicular to magnetic field lines, with an extended structure along them. Many poloidal Fourier harmonics, m, are coupled to provide the global mode structure, each of which is highly localised in the vicinity of the flux surface where the safety factor $q(r) = m/n$ is rational (n is the toroidal mode number). The spacing between these 'rational surfaces' is given by $\Delta = 1/nq'$ (where q' is the radial derivative of the safety factor profile). For high n modes thought to be responsible for micro-turbulence, $\Delta \ll L_{eq}$ where L_{eq} is the scale over which the equilibrium profiles vary. Adjacent magnetic flux surfaces are then approximately equivalent, and the ballooning formalism exploits this symmetry to reduce a 2D system (for the structure of the perturbed potential $\phi_1(x, \theta)$) to a pair of 1D ordinary differential equations [2, 3]. Expanding the global 2D equation in the small parameter $1/nq'$, at the lowest $n \to \infty$ ordering the ballooning theory provides the mode structure along a field line and the local mode eigenvalue $\Omega_0(x, k) = \omega_0(x, k) + \mathrm{i}\gamma_0(x, k)$. Here $x = r - r_0$ is the radial variable (r: radial coordinate, r_0: reference rational surface where $q(r_0) = m_0/n$) and $k = nq'\theta_0$ is the radial wavenumber (θ_0 corresponds to the poloidal angle θ where the individual Fourier modes are in phase, and therefore where the ballooning mode amplitude peaks). At this leading order θ_0 is a free parameter (and is generally chosen to maximise the instability growth-rate). To determine θ_0 and construct the full radial mode-structure and global (true) complex mode frequency $\Omega = \omega + \mathrm{i}\gamma$ from the leading order *local* results, we need to proceed to the next order in $1/nq'$. At this level, profile variations put a constraint on θ_0. Depending on the equilibrium profiles, this higher-order theory then predicts two types of global mode-structures for all toroidal microinstabilities [1, 6, 7]: the *Isolated Mode* (IM) and the *General Mode* (GM).

The IM exists in the special situation when $\Omega_0(x, k)$ has a stationary point in x and k. In typical up-down symmetric tokamak equilibria, this mode will balloon near the outboard-midplane (i.e. $\theta_0 = 0$) and have a strong global growth-rate $\gamma \approx \mathrm{Max}[\gamma_0]$. The GM on the other hand does not have any constraint on $\Omega_0(x, k)$ and is therefore always accessible. It will typically peak off the equatorial midplane, usually at the top or bottom of the poloidal cross-section, and has a growth-rate obtained by averaging Ω_0 over θ_0 (where Ω_0 is periodic in θ_0) [2, 7–9]. The GM is therefore more stable than the IM. Taylor expanding in x, $\Omega = \Omega_0(k) + \Omega_x(k)x + \Omega_{xx}(k)x^2/2 + \ldots$ (where Ω_x and Ω_{xx} denote the first and second radial derivatives), the IM exists under the condition $\Omega_x(k_0) = 0$, where $(\partial\Omega_x/\partial k)|_{k=k_0} = 0$. Here we point out that for a poloidally up-down symmetric equilibrium, periodicity in θ implies that $k_0 = 0$ satisfies this. More general

(for example, shaped) equilibria can result in non-zero values of k_0.

Now consider the situation in a transport barrier, such as the tokamak edge pedestal of the H-mode. We expect the source of free-energy for instabilities (i.e. the profile gradients) to be maximum somewhere inside that transport barrier. For some $r = r_0$ we therefore expect to find $\mathrm{Im}[\Omega_x]$=0, but in general $\mathrm{Re}[\Omega_x] \neq 0$ at this location, and the plasma cannot access the IM. Let us consider now the role of flow-shear, which is ubiquitous and likely to be important in the edge transport barrier [10–12]. A toroidal flow profile that is linear in x in the neighbourhood of r_0, $\Omega_\phi = \Omega'_\phi x$ (assuming a frame where $\Omega_\phi(r_0) = 0$), adds a radially varying Doppler shift to the local mode frequencies, such that $\Omega_x \to \Omega_x + n\Omega'_\phi$. Of course the flow-shear induced frequency shift Ω'_ϕ is real and there will be a critical flow-shear, $\Omega'_c = -\mathrm{Re}[\Omega_x]/n$, where $\Omega_0(x, k)$ has no term linear in x, triggering the IM. Dickinson *et al* [3] and Abdoul *et al* [13] have shown that such a transition does indeed occur for a critical flow-shear. The associated strong burst in linear growth and, likely, a corresponding burst in transport, could be responsible for small-ELMs.

While previous works have demonstrated the effect of *stationary* plasma profiles on the accessibility of these modes, the pedestal profiles in a tokamak plasma usually evolve continuously, crashing during the repetitive plasma eruptions called edge localised modes (ELMs), and then building up again towards the next ELM. Therefore, we are interested here in how the modes develop as the profiles evolve, particularly in the role of flow-shear. We are especially interested in the dynamics of the GM-IM-GM transition as this flow-shear evolves through the critical value referred to above. The resulting transient burst of growth during the IM phase may drive a plasma eruption which could provide a model for small-ELMs. The more typical "Type-I" ELMs are violent eruptions driven by ideal magneto-hydrodynamics (MHD) instabilities, and eject up to 10% of the stored plasma thermal energy. This would cause unacceptable damage on ITER; so techniques to control these Type-I ELMs or find "small-ELM" regimes relevant for ITER is very important. The physics of the GM-IM-GM transition that we explore here suggests a more benign ELM than the Type-I ideal-MHD event, providing a possible scenario for acceptable ELMs on ITER.

To explore the dynamics of the GM-IM-GM transition as flow-shear evolves, we carry out full 2D initial-value simulations of a model global ITG equation that captures the essential features of toroidicity and radial profiles generic to all toroidal micro-instabilities. In Section 2 we introduce this model before describing benchmark results for *stationary* profiles in Section 3, and the results for an *evolving* flow-shear in Section 4. We conclude in Section 5 with implications of our results and possible experimental tests for a small-ELM model based on this mechanism.

2. Model system

2.1. Physics model

In this paper we illustrate the essential physics by considering a simple global linear electrostatic fluid toroidal model of the ITG mode with adiabatic electrons for the perturbed potential $\tilde{\phi} = \phi_1(x,\theta)\exp(in\phi)$ in a large aspect-ratio circular cross-section tokamak [14]

$$\left[\rho_s^2\frac{\partial^2}{\partial x^2} - k_\theta^2\rho_s^2 - \frac{\sigma^2}{\Omega^2}\left(\frac{\partial}{\partial\theta} + \mathrm{i}nq\right)^2 - \frac{2\epsilon_n}{\Omega}\left(\cos\theta + \mathrm{i}\frac{\sin\theta}{k_\theta}\frac{\partial}{\partial x}\right) - \frac{\Omega-1}{\Omega+\eta_s}\right]\phi_1(x,\theta) = 0. \quad (1)$$

Here the first two terms containing ρ_s are due to finite Larmor radius effects; the third term is the ion-sound term and encapsulates the parallel dynamics; the fourth term arises due to the toroidal curvature; and the final eigenvalue term captures the adiabatic electron response, amongst other ion physics. The various equilibrium parameters used are as follows (prime denotes radial derivative): $\rho_s^2 = \rho_i^2\tau$, where ρ_i is the ion Larmor radius and $\tau = T_e/T_i$ the electron to ion temperature ratio; $\epsilon_n(r) = L_n/R$ is the density scale length $L_n(= n_s/n_s')$ normalised to the plasma major radius R; $\sigma(r) = \epsilon_n/(qk_\theta\rho_s)$; $k_\theta = m_0/r$ is the poloidal wavenumber, with $q(r_0) = m_0/n$ and n the toroidal mode number; $q = q(r_0) + q'x$ is the safety factor profile with $x = r - r_0$ and r_0 some reference rational surface; $\eta_s = (1+1.5\eta_i)/\tau$, where $\eta_i(r) = n_sT_i'/T_in_s'$ is the ITG mode drive; and finally, $\Omega = \omega + \mathrm{i}\gamma$ is the global mode frequency normalised to the electron diamagnetic frequency ω_{*e}.

In eqn. (1), balancing the eigenvalue term with the rest (which are small) requires either $\Omega \simeq 1$ or $\eta_s \gg 1$. The ordering $\Omega \simeq 1$ gives rise to the electron drift mode, whereas the condition $\eta_s \gg 1$ corresponds to the ITG branch [4] - which is the focus of our work. Note that because $\eta_s \gg 1$, we are constrained to consider only strongly unstable modes.

This model is, of course, a great simplification of the full ITG mode physics, which requires a gyrokinetic or gyrofluid treatment to take proper account of drift-resonances, and should also include electromagnetic effects particularly at high β [15]. Nevertheless, since we are more interested in the dynamics of the two toroidal eigenmode categories (IM and GM) than the details of any particular micro-instability, the use of this model, shown previously to analytically capture the two branches, is justified [2].

2.2. Numerical modelling

We solve eqn. (1) by Fourier expanding $\phi_1(x,\theta) = \sum_m \phi_m(x)\exp(-\mathrm{i}m\theta)$, and project out the Fourier harmonics to derive:

$$\left[b\hat{s}^2\frac{\partial^2}{\partial y^2} - b + \left(\frac{\sigma}{\Omega}\right)^2(m'-y)^2 - \frac{\Omega-1}{\Omega+\eta_s}\right]\phi_m = \frac{\epsilon_n}{\Omega}\sum_{\pm}\left[1 \pm \hat{s}\frac{\partial}{\partial y}\right]\phi_{m\pm1}. \quad (2)$$

Here $b = k_\theta^2\rho_s^2$, $m' = m - m_0$, $nq' = k_\theta\hat{s}$ ($\hat{s} = rq'/q$ is the magnetic-shear), and we have further defined the dimensionless radial variable $y = nq'x$ (note y takes integer

values at rational surfaces). This form also explicitly highlights the coupling of mode m with $m \pm 1$ modes, which is a result of the curvature drift term. Rather than solve this eigenmode equation, we develop a time-dependent system. But before discussing this formalism, let us consider the role of flow-shear.

2.2.1. Incorporating the effect of flow-shear Sheared perpendicular ($v'_\perp$) and parallel ($v'_\parallel$) flows are ubiquitous to the edge pedestal. In our analysis however, we consider the toroidal flows v_ϕ as dominant due to effects such as NBI driven toroidal momentum input, and strong neoclassical damping of poloidal flows [16]. So we set $v_\theta = 0$, and this constraint allows us to relate v_ϕ with $v_\perp$ - the perpendicular $E \times B$ shear provides a stabilisation mechanism and also convects the ballooning modes in the poloidal angle [17]. The impact of parallel velocity gradients on the linear drive [18] is neglected, assuming this is much smaller than the temperature gradient drive. As we will be considering flow-shears (normalised to ω_{*e}) of order $1/n$ to demonstrate the GM-IM-GM transition, this is a reasonable assumption. For such small flow-shears, the dominant effect is through a Doppler-shift in Ω [19], i.e. $\Omega \to \Omega + n\Omega'_\phi x$, where Ω'_ϕ is a real number and sets the flow-shearing rate. We are working in the reference frame where the rational surface of interest at $r = r_0$ is at rest. Centrifugal and Coriolis force effects can be neglected for the low rotation speeds we assume - much less than the sound speed. We shall be considering a time-dependent flow-shear in Section 4; nevertheless, we shall assume that the flow at the rational surface $r = r_0$ is fixed to avoid the complications associated with an accelerating frame of reference.

2.2.2. A time-dependent formalism We perform the transformation $\Omega \to \Omega + \gamma_E y$ to eqn. (2), where $\gamma_E = \mathrm{d}\Omega_\phi/\mathrm{d}q$, and map $\Omega \to \mathrm{i}\partial/\partial t$. We further decompose the potential into three new fields and evolve the system self-consistently in time using a 4^{th}-order Runge-Kutta scheme (refer to Appendix A for details). An instantaneous complex mode frequency $\Omega_m(t) = \mathrm{i}\partial \ln \phi_m/\partial t$ can be associated with each individual Fourier mode, evaluated at the rational surface where $q(r_m) = m/n$, i.e. at $y = m'$. Once an eigenmode is established, we expect $\Omega_m(t)$ to be the same for all m and independent of time.

2.3. Equilibrium parameters

Table 1 lists the physics parameters used in our simulations (deviations from these are mentioned where appropriate). In addition, the ITG drive η_s has a radial profile of the form $\eta_s = \eta_g(1.0 - \eta_c x^2)$, with $\eta_g = 2.0$, $\eta_c = 1062.5$, and 40 Fourier-modes on either side of m_0 are found to be sufficient for convergence.

For any given set of parameters, several radial harmonics of an eigenmode are simultaneously unstable. The initial-value code becomes dominated in time by the most unstable harmonic. To find the dominant linear mode more rapidly, we have chosen parameters where the most unstable harmonic has a significantly higher growth-rate

Table 1: Equilibrium parameters used in simulations, with frequencies normalised to ω_{*e}

r_0/a	$k_\theta \rho_i$	$\hat{s}$	ϵ_n	τ	q	n	m_0	γ_E
0.965	0.2	25.0	0.08	1.0	1.4	50	70	[-0.006, 0.006]

than the other modes, and is also close to the fundamental radial harmonic (further relaxing the grid resolution needed to resolve the finer spatial structures associated with higher harmonics). This means the solution will rapidly converge to the dominant mode from initial conditions, allowing for numerical efficiency and easy comparison with earlier eigenmode solutions to eqn. (1) [3]. Another guiding influence for our parameter choice is to ensure that the same eigenmode is the most unstable as the flow-shear is varied through the GM-IM-GM transition. This enables us to compare our initial-value code results readily with previous eigenmode studies. That said, and with small-ELM dynamics in mind, our parameters are relevant to those typically found in the pedestal (except, perhaps, η_s, which we must take to be large for the validity of the model).

3. Global mode behaviour: stationary profiles

For the results discussed in this section, all simulations were performed with plasma profiles held fixed in time. The simulations were initialised with noise, and after sufficient time, the initial-value code is seen to converge to an eigenmode solution (Fig. 1). Note how all the individual $\Omega_m(t)$ converge to a single global complex mode frequency Ω as the eigenmode establishes. Comparisons with the eigenmode solution of eqn. (2) developed in [3], over a wide range of plasma parameters, yields agreement with our initial value approach to within 0.1%.

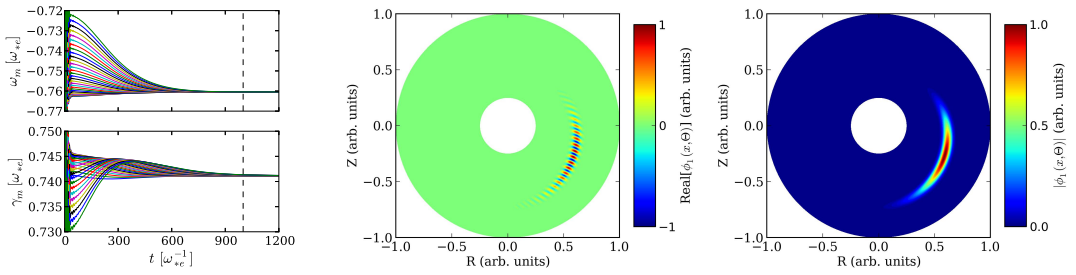

(a) (b) (c)

Figure 1: (Colour online) (a) shows the evolution of $\Omega_m(t) = \omega_m(t) + \mathrm{i}\gamma_m(t)$, where each line is a different poloidal harmonic m. (b) shows the real part of the eigenfunction in the poloidal plane corresponding to the time indicated (dashed vertical line) in (a), whereas (c) shows its magnitude. Note that the global mode peaks at $r_0/a = 0.965$; all our 2D plots have been scaled to help visualise the mode structure more clearly.

3.1. Obtaining the global eigenmodes: the Isolated and General Modes

We first set the flow-shearing rate $\gamma_E = 0$, and neglect all profile variations except for a quadratic η_s profile. As described in [3, 13], we then expect the IM which should balloon at the outboard-midplane (see Fig. 2b). The incorporation of flow-shear Doppler-shifts the real part of the complex mode frequency, removing the stationary point from the complex $\Omega_0(x)$. The IM is therefore no longer possible and the global eigenmode moves to peak away from the outboard midplane.

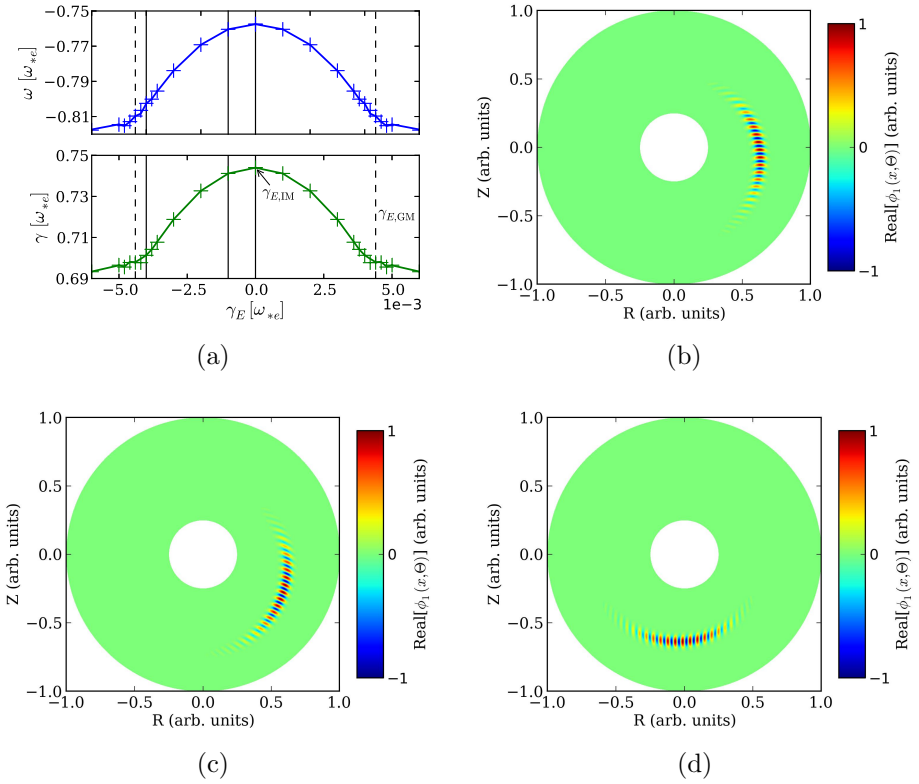

Figure 2: (Colour online) In (a), the solid curves show the *converged* eigenvalues from the initial-value code, whereas the crosses are solutions to the eigenmode eqn. (1) using the code from ref. [3]. The subsequent frames show how the IM (b) smoothly evolves (c) into the GM (d), as the flow-shear increases from $\gamma_E = 0$, through $\gamma_E = -0.001$ and finally to $\gamma_E = -0.004$, as indicated by the vertical lines in (a). The instability is a fully developed GM for $|\gamma_E| \geq \gamma_{E,\mathrm{GM}}$ (dashed lines in (a)).

Referring to Fig. 2a, the IM is seen to have the strongest growth. As the flow-shear magnitude is steadily increased towards $|\gamma_E| = \gamma_{E,\mathrm{GM}}$, the ITG growth-rate γ is reduced, and the IM is seen to smoothly evolve into the GM (Figs. 2b-2d), rotating from the outboard midplane at $\theta = 0$ for $\gamma_E = 0$ to the top/bottom at $\theta = \pm\pi/2$ for $|\gamma_E| > \gamma_{E,\mathrm{GM}}$. For our parameters $|\gamma_{E,\mathrm{GM}}| = 0.004$. The GM complex growth-rate is only weakly dependent on γ_E, and the transition to this asymptotic regime has been labelled by $\gamma_{E,\mathrm{GM}}$ in Fig. 2a. The IM therefore exists within a narrow window in γ_E, which, in our model, is in the vicinity of $\gamma_E = 0$. In general, as we introduce plasma

profiles (i.e. an x-dependence of q, ϵ_n etc.), the IM is accessed for a non-zero value of $\gamma_E = \gamma_{E,\mathrm{IM}}$ [13, 20].

Note the small difference between γ_{GM} and γ_{IM}. This is likely a result of the large aspect-ratio assumption ($\epsilon_n \ll 1$) and high magnetic shear, which favors the slab-like modes. For realistic geometries, we expect the Fourier modes to be more strongly coupled, leading to more highly unstable IMs compared to GM. But qualitatively, the results would be similar to those presented here.

3.2. Dynamics of eigenmode formation

One question that naturally arises is how do these linear eigenmodes establish their structures from a given set of initial conditions, and what are the associated dynamics of formation? But before exploring the physics in this subsection, we find it convenient to define a single instantaneous global growth-rate γ from an integral of the modulus of the potential over x and θ (see Appendix B).

Depending on how the perturbation is initialised, we observe three distinct scenarios for the formation of the eigenmode: (1) As illustrated in Fig. 3, if the initial perturbation peaks around the inboard-midplane, then independent of γ_E, the initial structure decays rapidly, and almost *simultaneously*, a transient double-structure is established near the outboard-midplane - this is not yet an eigenmode. Now if $|\gamma_E| < \gamma_{E,\mathrm{GM}}$, this double-structure combines into a single *coherent* eigenmode structure localised on the outboard side (at the midplane if $\gamma_E = \gamma_{E,\mathrm{IM}} = 0$). This is the situation shown in Fig. 3, where $\gamma_E = -0.0038 = -0.95\gamma_{E,\mathrm{GM}}$. Figures 2b and 2c give two further examples of the converged eigenmode structure for smaller values of $|\gamma_E| < \gamma_{E,\mathrm{GM}}$ ($\gamma_E = 0$ and -0.001). If however $|\gamma_E| \geq \gamma_{E,\mathrm{GM}}$, the coherent mode is convected poloidally and performs many poloidal rotations, before finally settling down to the eigenmode. This *Floquet* behaviour is distinguished by its periodic variation in $\gamma(t)$ (Fig. 4a), and will be described in more detail in Section 3.3. (2) If the perturbation is initialised anywhere on the outboard side, independent of γ_E, a strong single coherent structure first forms *at* the position of the initial perturbation, before being convected to its final eigenmode position. Figure 4b shows the evolution of the global growth-rate when the initial perturbation amplitude is maximum at the outboard-midplane. (3) Finally, when initialised with random noise distributed uniformly in the poloidal angle, a coherent structure first forms at the outboard-midplane *independent* of the size of γ_E. Next, and as with both previous scenarios, if $|\gamma_E| < \gamma_{E,\mathrm{GM}}$, the structure rotates to the poloidal position associated with its eigenmode and stays there, whereas if $|\gamma_E| \geq \gamma_{E,\mathrm{GM}}$, the coherent structure rotates continually to establish the Floquet Mode (Fig. 4c).

3.3. Floquet Modes

With the inclusion of sheared plasma rotation, the standard ballooning representation no longer captures the eigenfunction efficiently, as the sheared rotation destroys the underlying equivalence of adjacent magnetic rational flux surfaces. Cooper [21]

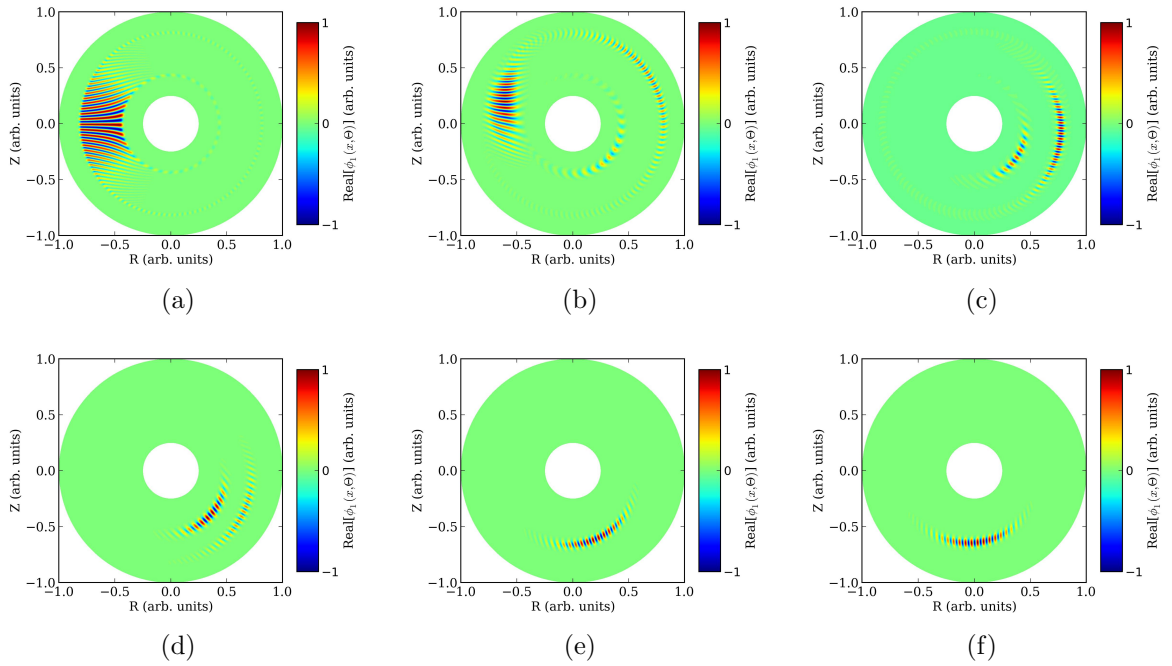

Figure 3: (Colour online) The plots show the poloidal mode-structure of the instability as it evolves towards a GM, after initiating the perturbation on the inboard side (to the left of each figure) with $\gamma_E = -0.95\gamma_{E,\mathrm{GM}}$. (a) shows the initial perturbation; (b)-(c) show the rapid formation of the outboard structure (only for $\gamma_E = \gamma_{E,\mathrm{IM}}$ does the final eigenmode establish here), accompanied by a decay of the initial inboard perturbation; and (d)-(f) show the subsequent evolution towards the GM. The frames correspond to the times 0T, 0.017T, 0.071T, 0.125T, 0.5T and 1.0T, where T is the eigenmode formation time.

addressed this by employing a time-dependent eikonal, which then leads to Floquet Modes. In ref. [22], Taylor and Wilson use an alternative eigenmode representation and conclude that, when higher-order $(1/n)$ effects are considered (as captured directly by these global simulations), a perturbation adopts a time-dependent Floquet form which evolves towards the eigenmode over $\sim n$ Floquet periods. Our simulations shed more light on this mechanism and we quantify this for specific cases.

We first establish the most unstable eigenmode for the parameters $\epsilon_n = 0.04$ and $\gamma_E = -0.003$, which is located near the bottom of the poloidal cross-section, as shown in Fig. 5b. We then re-start the simulation, and at $t = 200$, switch the flow-shear to $\gamma_E = 0.006$ instantly, and hold it fixed in time for the remainder of the simulation. Figure 5a shows how the global instantaneous Floquet Mode growth-rate, $\gamma_{\mathrm{FM}}(t)$, evolves in time in response to this change in γ_E. The eigenmode for this new shearing rate would be localised at the top of the plasma. However, instead of rotating poloidally to the top and staying there (Fig. 5c), the mode overshoots to the inboard side (Fig. 5d), then makes a *rapid* transition (Fig. 5e) to the outboard side (Fig. 5f), before again slowly tracking across the top; this rotation in the poloidal angle continues for many periods.

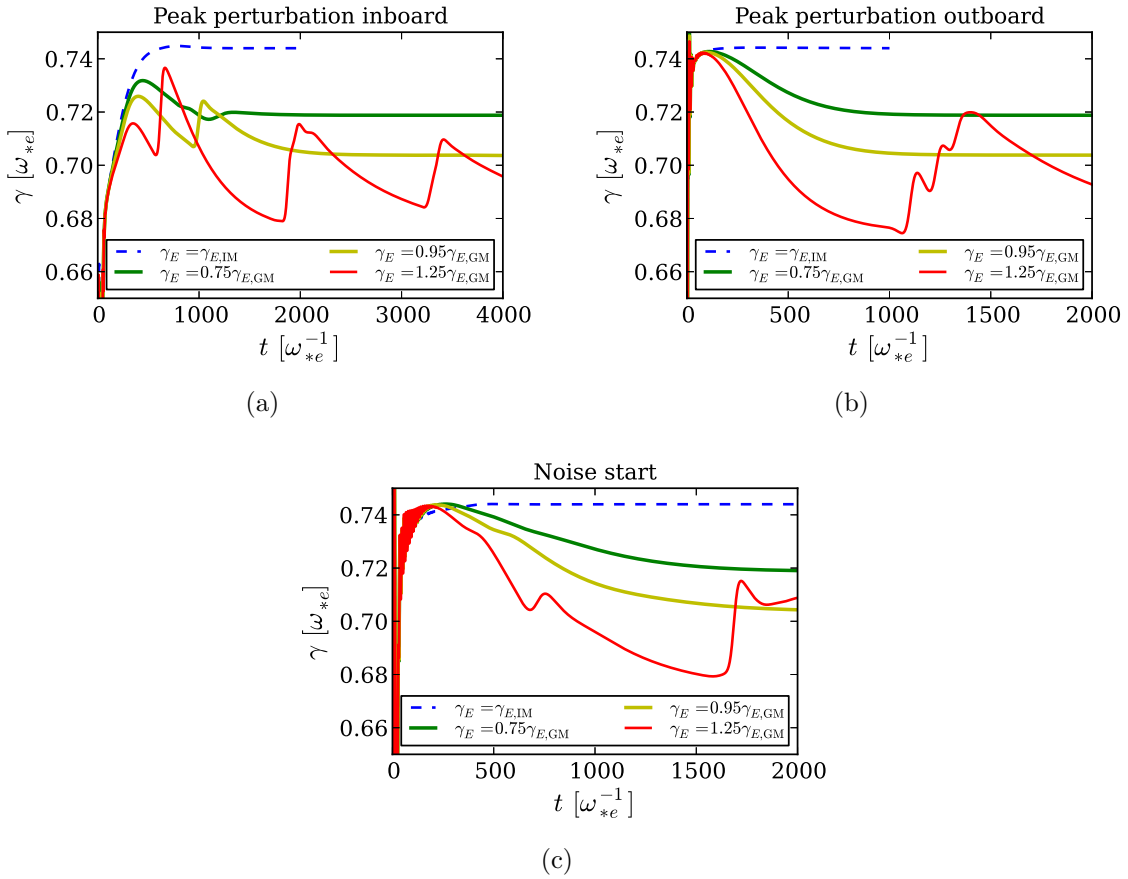

Figure 4: (Colour online) Evolution of the global growth-rates in time, as a function of the flow-shearing rate for different initial perturbations: (a) maximum amplitude on the inboard side; (b) maximum amplitude on the outboard side; and (c) poloidally uniform noise. For the case $\gamma_E = 1.25\gamma_{E,\mathrm{GM}}$, we just show the first few Floquet periods.

The final three plots (Figs. 5g, 5h, 5i) show a similar behaviour for the next Floquet period, except now the onset of the rapid outboard transition occurs closer to the top, and the mode whips even faster around the bottom. Further into the simulation, the evolving Floquet Mode gradually spends less time at the bottom and more time at the top with each cycle, before eventually settling down as a GM, with $\gamma_{\mathrm{FM}}(t) \to \gamma_{\mathrm{GM}}$ as predicted in ref. [22]. Our simulations suggest that the onset of this Floquet-like poloidal precession occurs when the flow-shear exceeds the threshold value, indicated by $\gamma_{E,\mathrm{GM}}$ in Fig. 2. For $|\gamma_E| \sim \gamma_{E,\mathrm{GM}}$, the instability goes to the top/bottom of the poloidal cross-section and stays there, but exceeding this value tips the mode into a Floquet oscillation.

Taylor and Wilson [22] further conclude that Floquet solutions evolve to the eigenmode over a time of order $n\kappa/\kappa_1$ Floquet periods, where the radial flow profile is given by $\kappa y + \kappa_1 y^2/n$. Note that in a higher-order treatment, even with $\kappa_1 = 0$, the radial variation in other equilibrium quantities typically contribute an $\mathcal{O}(n^{-2})$ piece to the quadratic term (such as $\eta_s(x)$), implying then that the Floquet Mode settles down

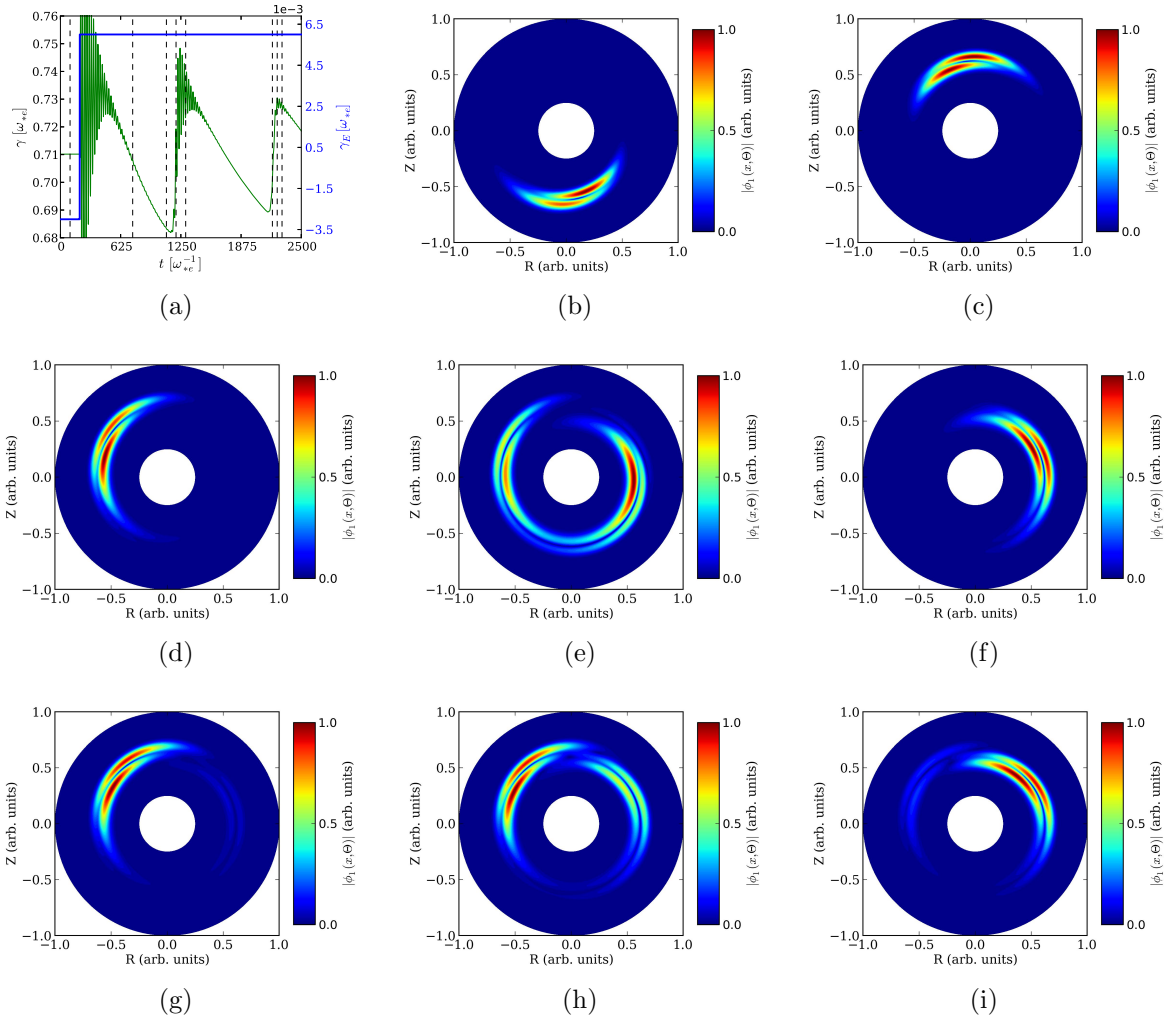

Figure 5: (Colour online) (a) shows the global growth-rate γ (green) and flow-shear γ_E (blue) as a function of the normalised time. The dashed vertical lines indicate time-slices that correspond to the potential plots presented in frames (b)-(i) in chronological order.

to the eigenmode after $\mathcal{O}(n^2)$ periods of rotation, as is the case in Fig. 5. Note also that ref. [22] analyses the electron-drift branch of eqn. (1). Nonetheless, we expect their conclusions will hold for all toroidal drift modes, in particular the ITG mode considered here; this is confirmed in Fig. 6. Each run is initialised with a perturbation on the outboard side, then performing scans in κ_1 at fixed κ and n, we find that the number of Floquet periods to converge to the eigenmode is indeed proportional to $n\kappa/\kappa_1$ (with the coefficient of determination $\mathrm{R}^2 = 0.97$). Note that for $n\kappa/\kappa_1 = -40$ and -100, Fig. 6b shows the classic Floquet behaviour. For $n\kappa/\kappa_1 = -30$ however, there is no Floquet behaviour, as the expected γ_E would have dropped below the $\gamma_{E,\mathrm{GM}}$ for these parameters.

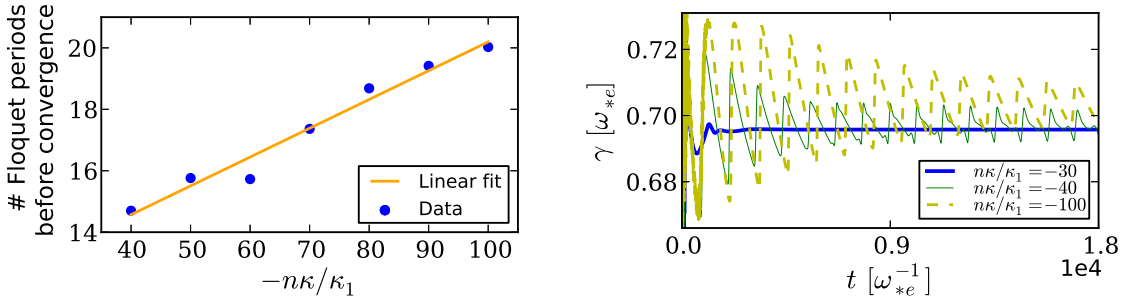

(a) (b)

Figure 6: (a) shows the number of Floquet periods required for the global growth-rate to converge to within 0.1% of the eigenmode growth-rate. (b) shows the evolution of the growth-rate in time for three different values of $n\kappa/\kappa_1$. Scans have been performed with fixed $\kappa = -0.005$, $n = 50$ and $\epsilon_n = 0.04$, while κ_1 was varied.

4. Global mode behaviour: dynamic profiles

The trigger for Type-I ELMs is well described by the ideal-MHD peeling-ballooning model [23, 24], and some other ELM types are qualitatively consistent with MHD triggers. For example, Type-II ELMs may be associated with pure-ballooning modes and the high/low density branches of Type-III may be explained using resistive-ballooning/pure-peeling triggers [25]. But are all ELMs necessarily MHD events? Or can the linear properties of toroidal drift modes provide an alternative model for some small-ELM types? In exploring whether such a model could explain small-ELMs, we are interested in how these modes would respond to evolving plasma profiles, particularly, as the flow-shear passes through a critical value that triggers the GM-IM-GM transition.

Since our interest is in the GM-IM-GM eigenmode transition as γ_E evolves from $-\gamma_{E,\mathrm{GM}}$, through $\gamma_{E,\mathrm{IM}}$ to $\gamma_{E,\mathrm{GM}}$, we choose to remove the Floquet dynamics from this study and initiate our simulations with an eigenmode that is close to a fully developed GM (ballooning at $\theta \sim -\pi/2$ for $\gamma_E = -0.95\gamma_{E,\mathrm{GM}}$). We then ramp the flow-shear through the critical value ($\gamma_E = \gamma_{E,\mathrm{IM}} = 0$ for our parameters) to access the IM, and then hold the flow-shear fixed (at $\gamma_E = 0.95\gamma_{E,\mathrm{GM}}$) to obtain another GM (ballooning now at $\theta \sim \pi/2$). The rate of change of flow-shear, $\mathrm{d}\gamma_E/\mathrm{d}t$, is then considered on three distinct time-scales: (1) a sufficiently slow change such that the instability retains its eigenmode form as it evolves in response to $\gamma_E(t)$, with $\mathrm{d}\gamma_E/\mathrm{d}t$ = 1.0e-6; (2) a much faster ramp with $\mathrm{d}\gamma_E/\mathrm{d}t$ = 1.0e-4; and (3), in the limiting case of $\mathrm{d}\gamma_E/\mathrm{d}t \to \infty$, i.e. a sudden switch in γ_E. We discuss these cases in turn.

4.1. Mode response to slowly varying profiles

If the equilibrium profiles vary sufficiently slowly, the linear modes have time to respond and retain the eigenmode structure corresponding to the *instantaneous* plasma parameters. Figure 7a represents this scenario. We know the evolving instability is an

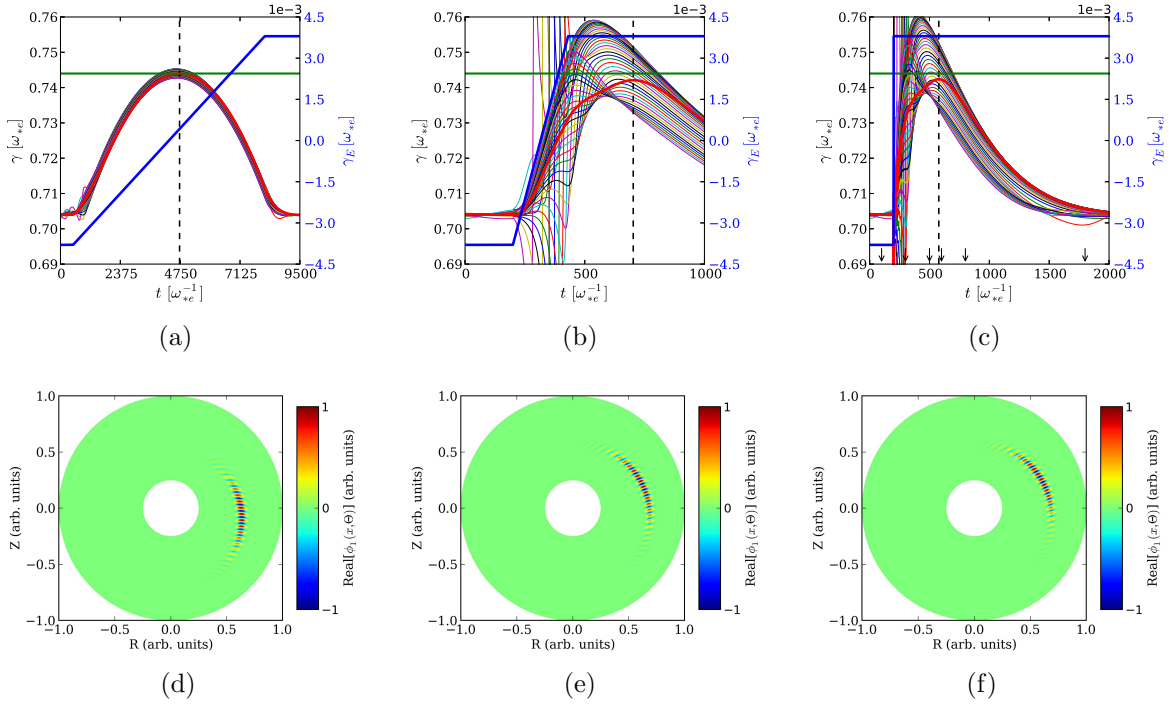

Figure 7: (Colour online) Plots (a)-(c) show the evolution of the growth-rate of each Fourier mode (coloured curves) as a function of flow-shear γ_E (solid blue) for different $\mathrm{d}\gamma_E/\mathrm{d}t$. (d)-(f) show the corresponding mode-structures at the times when the instantaneous global growth-rate is maximum, indicated by the dashed-vertical lines in the frames above. The green-horizontal line indicates the IM growth-rate, whereas the solid-red line is the instantaneous global growth-rate. Potential structures at the times annotated by the arrows in (c) can be seen in Fig. 8. [For $\omega_{*e} = 10^6$ Hz, 1000 units on the time-axis ~ 1 ms.]

eigenmode throughout since the plotted significant Fourier modes‡ have the same $\Omega_m(t)$ at all times. Figure 7d shows the eigenfunction at the time when the global growth-rate is the maximum (indicated by the dashed-vertical line in Fig. 7a). As expected, the mode balloons at $\theta = 0$ and has the same growth-rate as the IM for $\gamma_E = \gamma_{E,\mathrm{IM}} = 0$. Note that this scenario is similar to Fig. 2, where *each* value of γ, for the corresponding γ_E, was obtained by running the simulation to long times with profiles held fixed in time.

4.2. Mode response to rapidly varying profiles

Changing the flow-shear over a much quicker time-scale (Fig. 7b) in turn led to several interesting observations:

‡ The significant Fourier modes are defined to be those with an amplitude greater than 1% of the global-mode amplitude envelope.

Coherent identity: If the profiles change rapidly, the evolving instability can no longer retain its eigenmode identity. This is apparent from the different growth-rates $\gamma_m(t)$ associated with the significant Fourier harmonics (Fig. 7b). Nevertheless, the perturbation does retain a *coherent structure* as it rotates from the bottom of the plasma to the top with evolving γ_E. This characteristic is demonstrated in Fig. 8, but in the limit when $\mathrm{d}\gamma_E/\mathrm{d}t \to \infty$ (section 4.3).

Strong growth: Even though some Fourier harmonics can transiently have growth-rates greater than the IM, the global growth-rate as defined in Appendix B never exceeds γ_{IM} for the parameters considered, but does transiently approach it. This may be expected since the IM is obtained by combining the amplitudes and phases of the Fourier modes to yield the maximum growth-rate. What is intriguing, perhaps, is that $\gamma_{\max} \sim \gamma_{\mathrm{IM}}$ even though the structure is not exactly that of the eigenmode.

Profile lag: We observe that the growth-rate peaks, approaching that of the IM, somewhat after γ_E has passed through its critical value for the IM. Further, referring to Fig. 7e, we note that this maximum in growth-rate occurs after the mode has rotated past the outboard-midplane.

4.3. Mode response to a sudden profile switch

Finally, we ask what happens when the flow-shear passes through the critical value in the limit $\mathrm{d}\gamma_E/\mathrm{d}t \to \infty$, switching γ_E suddenly from negative to positive (Fig. 7c). We find that all the features discussed in Section 4.2 are recovered. Note also that the global growth-rate approaches γ_{IM} after only ~ 300 e-foldings, and then returns to the γ_{GM} value over a much longer period of ~ 1500 e-foldings. These numbers are approximately of the order it takes the IM and GM to establish their structures from noise.

4.4. Eigenmode-Floquet dynamics

So far, Floquet dynamics were removed from our GM-IM-GM transition studies by stopping the flow-shearing rate γ_E from going beyond $\gamma_{E,\mathrm{GM}}$. In Fig. 9a, we show that if γ_E is ramped beyond $\gamma_{E,\mathrm{GM}}$ at the same rate as for Fig. 7a, the mode develops into a Floquet Mode. If one ramps γ_E more slowly (so that the eigenmode can be treated in time more precisely) as in Fig. 9b, we find that the eigenmode performs two full Floquet cycles as γ_E exceeds $\gamma_{E,\mathrm{GM}}$, before settling to oscillate at the bottom of the tokamak (see γ around $t = 8.4\mathrm{e}4$ in Fig. 9c). We return to consider the possible implications of this in ELM dynamics in Section 5.

5. Summary and discussion

In the high-n limit, the higher-order ballooning eigenmode theory predicts two distinct linear mode structures (Isolated Mode and General Mode) for all toroidal

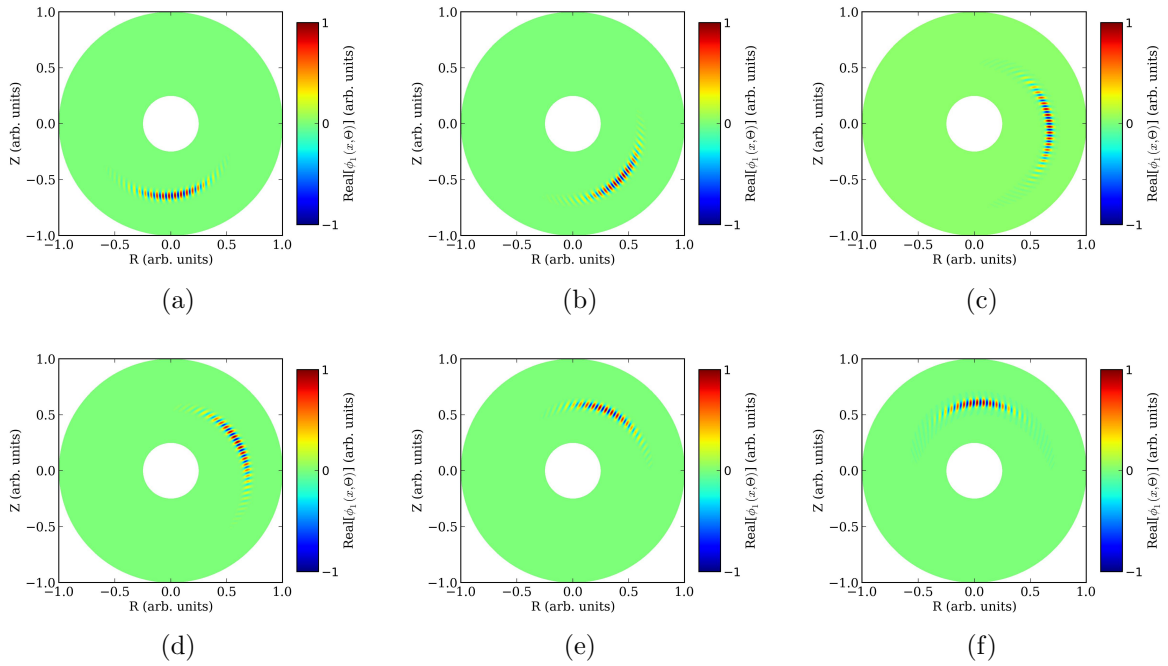

Figure 8: (Colour online) (a)-(f) show the poloidal mode-structure of the time evolving instability following a step in γ_E, with $\gamma_E < \gamma_{E,\mathrm{GM}}$ (chronologically at times indicated by arrows in Fig. 7c).

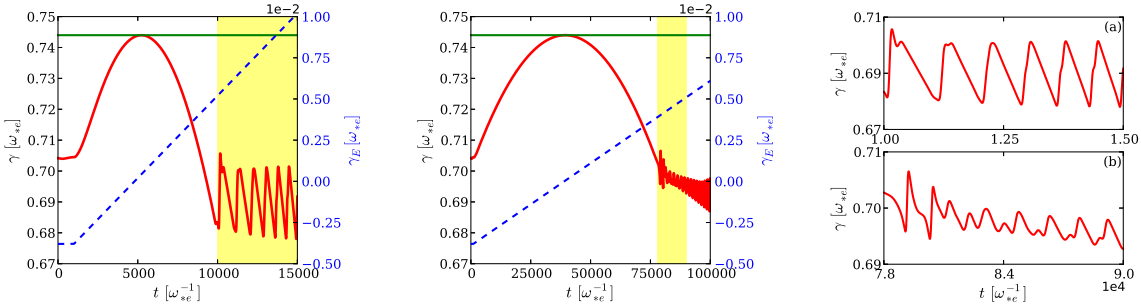

Figure 9: (a) shows the situation in Fig. 7a, except now the flow-shearing rate (dashed-blue line) has been pushed past $\gamma_{E,\mathrm{GM}}$; the case in (b) is for a much slower evolution of γ_E, with dγ_E/dt=1.0e-7. Plot (c) shows the magnified images of the shaded regions in (a) and (b).

microinstabilities (e.g. ITG, TEM, KBM etc.). In this paper we have presented results from a new time-dependent code, developed to investigate the properties of the linear global toroidal electrostatic fluid-ITG mode as the flow-shear evolves in time. While we consider the ITG mode as a specific example, we expect our results to be generic to most toroidal microinstabilities.

In Section 3, holding all plasma profiles fixed in time, we obtain both mode structures from our initial value approach and characterise their behaviour leading up

to the eigenmode formation. First, considering the eigenmode, we demonstrate that the GM, sitting at the bottom of the poloidal cross-section for a negative flow-shear, rotates to the top for a positive flow-shear, accessing the IM on the outboard side for an intermediate critical flow-shear. Note that if the direction of the curvature and ∇B drifts are reversed, the GM will then balloon at the bottom (top) for a positive (negative) flow-shear. It is interesting to note that Brower *et al* [26] in their study of the spatial and spectral distribution of tokamak microturbulence, observe a strong up-down asymmetry in the poloidal density fluctuation distribution along a vertical chord passing through the plasma centre, which inverts with current reversal. This could be connected to the presence of General Modes. Second, we find that for our strongly unstable cases, the GM structure takes ~ 1300 e-foldings to form from noise, while the IM takes a considerably less ~ 300 e-foldings§. These values indicate that in this case, non-linear terms are likely to become important before the linear mode-structures can establish. However, we remind the reader that our model is constrained to consider only strongly unstable modes (since $\eta_s \gg 1$). As we gradually increase η_s by 100%, we find that the global growth-rate increases by over 80%, whereas the time to form the eigenmode only changes by 0.1%. Future studies should test our ideas in a more realistic plasma model - if the time to form the eigenmode remains insensitive to the linear drive when profiles are held close to marginal stability, then our linear dynamics may play an important role in the turbulence close to the linear threshold. Thirdly, for high linear flow-shears κ (equivalently, γ_E), we find the instability exhibits Floquet behaviour. The addition of a quadratic flow-profile $\kappa_1 y^2/n$ damps the Floquet oscillations so that $\gamma_{\rm FM}(t)$ approaches $\gamma_{\rm GM}$, as the Floquet Mode evolves towards the eigenmode, over $\mathcal{O}(n\kappa/\kappa_1)$ Floquet periods; this is in agreement with the theoretical predictions in ref. [22].

In Section 4, we investigated the response of these toroidal drift modes as the flow-shear is evolved through a critical value to trigger a GM-IM-GM transition. For small deviations from the critical flow-shear, i.e. $|\gamma_E| < \gamma_{E,\rm GM}$, the flow profile was changed over three time-scales. When the flow is varied on a slow time-scale compared to the eigenmode formation time, as the mode structure responds, it retains the instantaneous eigenmode form. However, when the flow-profile was changed more rapidly, and subsequently in the limiting case of $\mathrm{d}\gamma_E/\mathrm{d}t \to \infty$, several interesting features emerge: (1) the evolving instability is no longer an eigenmode, but nevertheless maintains a coherent structure which is convected poloidally throughout the flow-ramp; (2) despite not being an eigenmode, we find the peak growth-rate $\gamma_{\rm max} \sim \gamma_{\rm IM}$; (3) there is a noticeable lag with $\gamma_{\rm max}$ realised some time after the profiles pass through the critical γ_E (which would give the IM for flows held fixed in time); and (4) the peak in growth-rate occurs when the mode structure has rotated slightly beyond the outboard-midplane. Next when the flow-shear is taken into the $|\gamma_E| > \gamma_{E,\rm GM}$ regime, the presence of Floquet transients seem ubiquitous to our system. The parameter $(\mathrm{d}^2\Omega_\phi)/(\mathrm{d}q\mathrm{d}t)$ strongly influences the eigenmode-Floquet dynamics and determines how closely the

§ These timescales are found to be broadly similar for a range of initial conditions.

instability tracks an eigenmode.

A model for small-ELMs? The large Type-I ELMs driven by ideal-MHD instabilities would cause excessive erosion in ITER, so it is important to either develop control systems for these ELMs, or identify ITER-relevant (e.g. low collisionality) small/no-ELM regimes. The small Grassy-ELM regime is a possible option, but in the absence of a physics-based model, the relevance for ITER remains uncertain. This Grassy-ELM regime observed in JT-60U appears to be influenced by flows [27], providing ELMs with characteristic frequencies between $\sim 400 - 1500$ Hz. Could a GM-IM-GM transition as the profiles evolve provide a burst of instability corresponding to small-ELMs such as these? One mechanism arises when the pedestal conditions are such that γ_E passes through $\gamma_{E,\mathrm{IM}}$ before reaching the ideal-MHD stability boundary. This would trigger an IM, and the resulting burst of transport might be associated with an ELM. Furthermore, the rapid adjustment of profiles would re-establish the GM and terminate the ELM crash, limiting the energy released, and allowing the cycle to repeat. The observation of Floquet Modes in Fig. 9 as the flow-shear is ramped beyond $\gamma_{E,\mathrm{GM}}$ and the GM establishes may further influence the dynamics of ELMs.

These results, although based on a relatively simple fluid-ITG model, are expected to be generic for all types of toroidal micro-instabilities, and thus provide some robust experimentally testable predictions. For example, density/potential/magnetic fluctuation measurements inside the pedestal viewed over a wide poloidal angle should indicate asymmetries about the mid-plane, which would typically reverse when the direction of the ∇B drift is reversed. Further, if some small-ELM types are indeed triggered by the GM-IM-GM transition, data from the above diagnostic, resolved temporally between successive small-ELM bursts, should indicate fluctuations that shift poloidally at the time of ELM onset.

We note that in this paper, the parameter that controls the transition between the GM and the IM is an *externally imposed* toroidal flow-shear. However, there is strong evidence of *intrinsic* toroidal rotation in tokamaks [28], a likely source of which could be turbulent fluctuations themselves [29–31]. A self-consistent, coupled system that accounts for the feedback of the turbulence on the flows will be explored in the future. Furthermore, it is important to explore these self-consistent dynamics in a realistic situation where profiles are close to the GM marginal stability (e.g. for the kinetic ballooning mode). This will require studies of more complete gyrokinetic models (e.g. [32]) that retain more physics than our reduced fluid model. As a final remark, we note that these ideas ultimately need to be tested non-linearly to explore the interaction of turbulence with flows.

Appendix A. Relation of fields in the presence of flow-shear

We start with eqn. (2) and perform the transformation $\Omega \to \Omega + f$, where $f = \gamma_E y$ is the Doppler-shift due to the flow-shear. We further define three new fields $G_m = \Omega\phi_m$, $H_m = \Omega G_m$ and $F_m = \Omega H_m$. This allows eqn. (2) to be written in a differential-

difference form:

$$\hat{\alpha}F_m = -\left(\hat{\Delta}\phi_m + \hat{\beta}H_m + \hat{\Gamma}G_m\right) + \epsilon_n[\kappa_H + \kappa_G(2f + \eta_s) + \kappa_\phi(f^2 + \eta_s f)] \tag{A.1}$$

The spatial operators in the absence of flow-shear are defined in table A1, which we use to define the operators acting on the fields in the presence of flow-shear in table A2.

Table A1: Spatial operators in the absence of plasma flow

α	$b\hat{s}^2\partial_y^2 - (b+1)$
β	$\eta_s(b\hat{s}^2\partial_y^2 - b) + 1$
Γ	$\sigma^2(m' - y)^2$
Δ	$\eta_s\sigma^2(m' - y)^2$
$\phi_\pm$	$\phi_{m+1} \pm \phi_{m-1}$
κ_ϕ	$\phi_+ + \hat{s}\partial_y\phi_-$
κ_G	$G_+ + \hat{s}\partial_y G_-$
κ_H	$H_+ + \hat{s}\partial_y H_-$

Table A2: New operator definitions upon the incorporation of a flow-profile f

$\hat{\alpha}$	α
$\hat{\beta}$	$\beta + 3f\alpha$
$\hat{\Gamma}$	$\Gamma + 2f\beta + 3f^2\alpha$
$\hat{\Delta}$	$\Delta + f\Gamma + f^2\beta + f^3\alpha$

Next transforming $\Omega \to \mathrm{i}\partial/\partial t$, we see

$$\frac{\partial}{\partial t}\begin{pmatrix} \phi_m \\ G_m \\ H_m \end{pmatrix} = -\mathrm{i}\begin{pmatrix} G_m \\ H_m \\ F_m \end{pmatrix}, \tag{A.2}$$

which we solve using the 4^{th}-order Runge-Kutta scheme, with F_m calculated consistently at every time-step by inverting eqn. A.1.

Appendix B. Calculating a global growth-rate from potential

For an eigenmode formulation we may write:

$$\phi(x,\theta,t) = e^{-\mathrm{i}\Omega t}\sum_m \phi_m(x)e^{-\mathrm{i}m\theta} \tag{B.1}$$

$$= e^{-\mathrm{i}\Omega t}\hat{\phi}. \tag{B.2}$$

Multiplying with its complex-conjugate we have

$$|\phi|^2 = e^{2\gamma t}|\hat{\phi}|^2, \tag{B.3}$$

where

$$|\hat{\phi}|^2 = \left(\sum_m \phi_m e^{-\mathrm{i}m\theta}\right)\left(\sum_k \phi_k^* e^{\mathrm{i}k\theta}\right) \quad . \tag{B.4}$$

Integrating over the poloidal cross-section $\langle ... \rangle_\theta$ and in x provides

$$|\phi| = \left\langle |\phi|^2 \right\rangle_{\theta,x}^{1/2} = e^{\gamma t}\sqrt{2\pi}\sqrt{\sum_m \int_x |\phi_m|^2 \mathrm{d}x} \quad ,$$

from which we derive the global growth-rate:

$$\gamma = \frac{1}{|\phi|}\frac{\partial |\phi|}{\partial t} \quad .$$

Acknowledgments

This work has been carried out within the framework of the EUROfusion consortium and has received funding in part from the EURATOM research and training programme 2014-18 grant [633053], the RCUK Energy Programme [EP/I501045], the EPSRC DTN grant [EP/K504178/1] and the Overseas Research Scholarship, University of York. The views and opinions expressed herein do not necessarily reflect those of the funding bodies. AB would like to thank Peshwaz Abdoul, Jarrod Leddy and Jonathan Skipp for many helpful discussions. DD was supported by a EUROfusion fusion researcher fellowship [WP14-FRF-CCFE/Dickinson]. HRW is the holder of a Royal Society Wolfson Research Merit Award. The code is available by request from the University of York Data Catalogue http://dx.doi.org/10.15124/b3b40ad0-152a-4b04-90e5-3460e7d5a487.

References

[1] Connor J W, Taylor J B and Wilson H R 1993 *Phys. Rev. Lett.* **70**(12) 1803–1805
[2] Taylor J B, Wilson H R and Connor J W 1996 *Plasma Physics and Controlled Fusion* **38** 243
[3] Dickinson D, Roach C M, Skipp J M and Wilson H R 2014 *Physics of Plasmas* **21** 010702
[4] Wesson J 2011 *Tokamaks* (Oxford University Press Inc., New York: Oxford University Press)
[5] Mantica P, Strintzi D, Tala T, Giroud C, Johnson T, Leggate H, Lerche E, Loarer T, Peeters A G, Salmi A, Sharapov S, Van Eester D, de Vries P C, Zabeo L and Zastrow K D 2009 *Phys. Rev. Lett.* **102**(17) 175002
[6] Taylor J B, Connor J W and Wilson H R 1993 *Plasma Phys. Control. Fusion* **35** 1063
[7] Dewar R L 1997 *Plasma Physics and Controlled Fusion* **39** 453
[8] Waelbroeck F L and Chen L 1991 *Physics of Fluids B* **3** 601–610
[9] Miller R L, Waelbroeck F L, Hassam A B and Waltz R E 1995 *Physics of Plasmas* **2** 3676–3684
[10] Biglari H, Diamond P H and Terry P W 1990 *Physics of Fluids B* **2** 1–4
[11] Hahm T S and Burrell K H 1995 *Physics of Plasmas* **2** 1648–1651
[12] Terry P W 2000 *Rev. Mod. Phys.* **72**(1) 109–165
[13] Abdoul P A, Dickinson D, Roach C M and Wilson H R 2015 *Plasma Phys. Control. Fusion* **57** 065004
[14] Connor J W and Taylor J B 1987 *Physics of Fluids* **30** 3180–3185
[15] Candy J 2005 *Physics of Plasmas* **12** 072307
[16] Hassam A B and Kulsrud R M 1978 *Physics of Fluids* **21** 2271–2279
[17] Waltz R E, Dewar R L and Garbet X 1998 *Physics of Plasmas* **5**
[18] Roach C M, Abel I G, Akers R J, Arter W, Barnes M, Camenen Y, Casson F J, Colyer G, Connor J W, Cowley S C, Dickinson D, Dorland W, Field A R, Guttenfelder W, Hammett G W, Hastie R J, Highcock E, Loureiro N F, Peeters A G, Reshko M, Saarelma S, Schekochihin A A, Valovic M and Wilson H R 2009 *Plasma Physics and Controlled Fusion* **51** 124020

[19] Connor J W and Martin T J 2007 *Plasma Phys. Control. Fusion* **49** 1497
[20] Hill P, Saarelma S, McMillan B, Peeters A and Verwichte E 2012 *Plasma Phys. Control. Fusion* **54** 065011
[21] Cooper W A 1988 *Plasma Physics and Controlled Fusion* **30** 1805
[22] Taylor J B and Wilson H R 1996 *Plasma Phys. Control. Fusion* **38** 1999
[23] Connor J W, Hastie R J, Wilson H R and Miller R L 1998 *Physics of Plasmas* **5** 2687–2700
[24] Snyder P B, Wilson H R, Ferron J R, Lao L L, Leonard A W, Osborne T H, Turnbull A D, Mossessian D, Murakami M and Xu X Q 2002 *Physics of Plasmas* **9** 2037–2043
[25] Wilson H R, Cowley S C, Kirk A and Snyder P B 2006 *Plasma Physics and Controlled Fusion* **48** A71
[26] Brower D L, Peebles W A, Luhmann N C and Savage R L 1985 *Phys. Rev. Lett.* **54**(7) 689–692
[27] Oyama N, Sakamoto Y, Isayama A, Takechi M, Gohil P, Lao L, Snyder P, Fujita T, Ide S, Kamada Y, Miura Y, Oikawa T, Suzuki T, Takenaga H, Toi K and the JT-60 Team 2005 *Nuclear Fusion* **45** 871
[28] Rice J, Ince-Cushman A, deGrassie J, Eriksson L G, Sakamoto Y, Scarabosio A, Bortolon A, Burrell K, Duval B, Fenzi-Bonizec C, Greenwald M, Groebner R, Hoang G, Koide Y, Marmar E, Pochelon A and Podpaly Y 2007 *Nuclear Fusion* **47** 1618
[29] Dong J Q, Horton W, Bengtson R D and Li G X 1994 *Physics of Plasmas* **1** 3250–3261
[30] Coppi B 2002 *Nuclear Fusion* **42** 1
[31] Diamond P, Kosuga Y, Grcan , McDevitt C, Hahm T, Fedorczak N, Rice J, Wang W, Ku S, Kwon J, Dif-Pradalier G, Abiteboul J, Wang L, Ko W, Shi Y, Ida K, Solomon W, Jhang H, Kim S, Yi S, Ko S, Sarazin Y, Singh R and Chang C 2013 *Nuclear Fusion* **53** 104019
[32] Hahm T S, Wang L and Madsen J 2009 *Physics of Plasmas* **16** 022305